Modeling and Optimization with Viscoelastic Differential Constitutive Models

Kristian Ejlebjerg Jensen[1], Peter Szabo[2], Manuel A. Alves[2] and Fridolin Okkels[1]

[1] Technical University of Denmark, Department of Micro- and Nanotechnology, TSMO
[2] Technical University of Denmark, Department of Chemical and Biochemical Engineering
[3] University of Porto, Faculty of Engineering, Department of Chemical Engineering, CEFT

ABSTRACT

We present a combination of a free form optimization method with a set of differential constitutive equations for viscoelastic flow. We apply this tool on the phenomena of anisotropic flow resistance and bistability, both due to viscoelastic effects. In the case of anisotropic flow resistance we find a novel material layout that promises superior performance in the regime of moderate viscoelasticity, when compared to previous designs, and we have indeed been able to confirm this hypothesis experimentally. Our results related to bistable behaviour are purely numerical and specific to the cross-slot geometry. We optimize features related to the bistability, and since this appears implicitly, we adopt a heuristic approach based on dissipation ratios. The optimized design features contractions for and as such it supports the layout used in experimental devices.

INTRODUCTION

Many qualitative features of viscoelastic flow in complex geometries can be reproduced with continuum models based on differential constitutive equations as demonstrated by Baaijens et al.[1]. Recent models developments due to Fattal and Kupferman[2] have improved robustness as well as overall usability of these models to the point, where we have been able to combine such a model with a free-form optimization method (e.g. capable of introducing obstacles). The work relies heavily on a commercial high level finite element package (COMSOL) and related implementation of the optimization method by Olesen et al.[3].

Although we would like to applaud the general progress within modeling of viscoelastic fluids in complex geometries, we would also like to stress that the models remain computationally intensive due to the presence of two tensor variables. In example, the 3D simulations by Sahin[4] were carried out on supercomputers and, even then, only in simple benchmark geometries. Furthermore, computations in the regime of high viscoelasticity is limited by the presence of small time- and length scales in what is collectively referred to as viscoelastic turbulence, no viscoelastic turbulence models exists. The results presented in the following are thus limited to steady 2D flow in the regime of low to moderate viscoelasticity.

Anisotropic flow resistance due to viscoelastic effects can be used for microfluidic valves without moving parts. The lack of moving parts allows for a robust working mechanism at the cost of leaks in the sense that the fluid is allowed to pass in both flow directions, but the direction dependent resistance can still be utilized in the context of pumping as demonstrated with anisotropic flow resistance due to

inertial effects by Stemme and Stemme[5]. Inertial effects however vanish as devices are scaled down, and this constitutes the motivation for pursuing viscoelastic valves. Previous experimental designs by Nguyen et al.[6] (and references therein) have been a type of contraction geometry, while the design we find theoretically[7] and test experimentally[8] depends on the combination of a contraction with an obstacle.

The cross-slot geometry can be used to produce extensional flow, which is interesting in the context of microrheometry as remarked by Galindo-Rosales et al.[9]. It has been established experimentally by Arratia et al.[10] and using simulations by Rocha et al.[11] that the geometry can cause bistability in the form of a pitchfork bifurcation. The simulations also indicate that the flow resistance has a kink at the point of bistability. Furthermore they allow forcing of an unstable symmetric solution beyond the point of bistability, and careful analysis reveals that the asymmetric bifurcated solution gives rise to a reduction in hydraulic resistance. We use this observation to formulate a heuristic objective function that relates to optimization of early bistability.

MODELING

The starting point of modeling viscoelastic flow is the Navier-Stokes equation

$$\rho\left(\frac{\mathrm{D}\boldsymbol{v}}{\mathrm{Dt}}\right) = \boldsymbol{\nabla}\cdot\left(-\underline{\underline{\boldsymbol{I}}}p + \eta_s\underline{\underline{\dot{\boldsymbol{\gamma}}}} + \underline{\underline{\boldsymbol{\tau_p}}}\right) - \alpha\boldsymbol{v},$$
$$\text{and} \qquad 0 = \boldsymbol{\nabla}\cdot\boldsymbol{v},$$

where D is the material derivative, $\underline{\underline{\dot{\boldsymbol{\gamma}}}} = \boldsymbol{\nabla v} + (\boldsymbol{\nabla v})^{\boldsymbol{T}}$ is the symmetric rate of strain tensor, ρ is the density, $\boldsymbol{v}$ is the velocity, p is the pressure, $\underline{\underline{\boldsymbol{I}}}$ is the identity matrix, η_s is the solvent viscosity, $\underline{\underline{\boldsymbol{\tau_p}}}$ is the elastic stress tensor and α is the inverse permeability. The elastic stress tensor is specific to viscoelastic fluids, while the damping term $-\alpha\boldsymbol{v}$ is related to the optimization method, i.e. it vanishes in fluid regions and dominates in solid regions. This paper focuses on a dumbbell model, that is the elastic properties of the fluid is approximated by an ensemble of point masses that are connected pair wise by springs. The extension and orientation of such an elastic dumbbell can be described by its end-to-end vector $\boldsymbol{a}$, which defines the conformation tensor

$$\underline{\underline{\boldsymbol{A}}} = \frac{\langle \boldsymbol{a}\otimes\boldsymbol{a}\rangle}{a_{eq}^2},$$

where $\mathrm{a_{eq}}$ is the equilibrium extension of the spring and $\langle \ldots \rangle$ is a statistical average. When the fluid is at rest the conformation tensor thus equals the identity matrix, otherwise it gives rise to a non-zero elastic stress

$$\underline{\underline{\boldsymbol{\tau_p}}} = \frac{\eta_p k(\underline{\underline{\mathbf{A}}})}{\lambda}\left(\underline{\underline{\mathbf{A}}} - \underline{\underline{\mathbf{I}}}\right), \text{ and}$$
$$k(\underline{\underline{\mathbf{A}}}) = \frac{1}{1-\mathrm{Tr}(\underline{\underline{\mathbf{A}}})/{a_{\max}}^2}.$$

where λ is the dumbbell relaxation time and η_p is the polymer viscosity, $k(\underline{\underline{\mathbf{A}}})$ is a nonlinear spring constant modification that sets an upper bound, ${a_{\max}}^2$ on the trace of the conformation tensor.

The evolution equation for the conformation tensor contains terms due to convection, relaxation and deformation ($\underline{\underline{\mathbf{def}}}$);

$$\frac{D\underline{\underline{\mathbf{A}}}}{Dt} = -\frac{k(\underline{\underline{\mathbf{A}}})}{\lambda}\left(\underline{\underline{\mathbf{A}}} - \underline{\underline{\mathbf{I}}}\right) + \underline{\underline{\mathbf{def}}}\left(\underline{\underline{\mathbf{A}}}, \boldsymbol{\nabla v}\right)$$
$$\underline{\underline{\mathbf{def}}}\left(\underline{\underline{\mathbf{A}}}, \boldsymbol{\nabla v}\right) = \underline{\underline{\mathbf{A}}}\cdot\boldsymbol{\nabla v} + (\boldsymbol{\nabla v})^T\cdot\underline{\underline{\mathbf{A}}}$$

Note that the relaxation term with $k(\underline{\underline{\mathbf{A}}})$ will tend to dominate the equation as the trace of the conformation tensor approaches L^2. This model is called the finite extensibility model due to Chilcott and Rallison (FENE-CR). It has a constant shear

viscosity, and it is inspired from the FENE-P model, which has shear thinning behavior.

We solve the equation system by initializing a transient solver with the solution of a Newtonian fluid. After evolving the equation for many relaxation times, we use the final transient solution as initial guess to a stationary solver.

TOPOLOGY OPTIMIZATION

Topology optimization is different from traditional parametric optimization in the sense that the design is described by a field θ, which is zero in solid areas and 1 in fluid areas rather than a set of variables chosen by the user. The numerical discretization of the computational domain thus determines not only the number design variables, but also the local resolution of the design variable field. A continuum optimization problem can then be formulated by allowing for intermediate design variables and thus also areas that are neither fluid nor solid, but rather something sponge like. Such sponge like areas can be described with the damping force $-\alpha \boldsymbol{v}$ mentioned in the modeling section. Since sponge-like areas are difficult to realize in practice, they should ideally only appear in the temporary designs of the optimization and not in the final converged design.

We are interested in optimizing devices relying on viscoelastic effects, but it is well known that the magnitude of viscoelastic effects increases at small length scales and the very nature of our optimization problems thus has the potential to result in designs with length scales identical to the that of the numerical discretization. This entails not only poor, if not unphysical, numerical approximation of the governing equation, but also risk of unsteady flow, the presence of which cannot be handled by the applied optimization implementation. Consequently we wish to impose a lower bound $L_{\min}$ on the length scale of the design, and this can be achieved by imposing the PDE filter of Lazarov and Sigmund[12]

$$L_{\min}^2 \tilde{\nabla}^2 \tilde{\theta} = \tilde{\theta} - \theta,$$

where $\tilde{\theta}$ is the filtered design variable. The filter unfortunately also gives rise to larger areas of intermediate design variables with sponge like material and therefore a projected function is often applied

$$\bar{\theta} = \frac{1}{2} + \frac{\tanh\left(\xi\left(\tilde{\theta} - \frac{1}{2}\right)\right)}{2\tanh(\xi/2)},$$

where ξ is a parameter controlling steepness of the projection. Finally the damping term is defined in terms of the projected design variable $\bar{\theta}$ using a convex relation

$$\alpha(\bar{\theta}) = \alpha_{\max}\left(1 - \bar{\theta}\frac{(1+q)}{\bar{\theta}+q}\right),$$

where q controls the convexity and $\alpha_{\max}$ is the damping in solid regions. Ideally ξ, $\alpha_{\max}$ and q should be as large as possible, while the filter length $L_{\min}$ should be small. The convexity of the optimization problem however decreases in these limits. We have found a set of parameters that facilitates a good compromise between acceptable approximation of the physics in solid and fluid areas as well as an objective found that is smooth with respect to variations of the design variables

$$L_{\min} = h_{\text{mesh}}, \qquad \xi = 10,$$
$$q = 4 \cdot 10^{-6} \text{ and } \mathrm{Da} = \frac{\eta_s + \eta_p}{L^2 \alpha_{\max}} = 10^{-5},$$

where the Darcy number Da has been introduced in terms of the characteristic length scale L. It describes the magnitude of viscous forces relative to damping forces in solid regions, and it thus belongs among the other numerical parameter. Should a design without a steady solution appear, we use the final transient solution to calculate the derivative of the objective function. This gradient is used to improve the design in an

iterative way using the method of moving asymptotes by Svanberg[13].

ANISOTROPIC FLOW RESISTANCE

The setup for optimization of anisotropic flow resistance is sketched fig. 1. The flow is pressure driven with noslip boundary conditions at the upper and lower walls, open conditions periodic conditions at the sides and a central domain in which the design variables are defined. The flow is calculated with a pressure drop from left to right and vice versa.

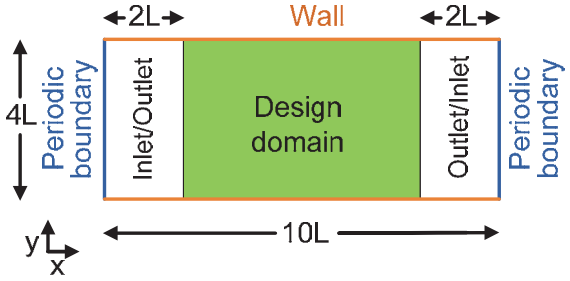

Figure 1. The optimization problem is sketched in terms of boundary conditions, domains and the length scale L.

The objective function ϕ is taken as the ratio of flow rates $\dot{V}$ between these two solutions (← and →)

$$\phi = \frac{\dot{V}_{\leftarrow}}{\dot{V}_{\rightarrow}} = \frac{\int -\boldsymbol{v}_{\leftarrow}\cdot\hat{\boldsymbol{x}}d\boldsymbol{r}}{\int \boldsymbol{v}_{\rightarrow}\cdot\hat{\boldsymbol{x}}d\boldsymbol{r}}.$$

We wish to avoid a working mechanism related to inertial effects and thus use the following physical constants

$$\mathrm{Re} = \frac{\{\text{inertial effects}\}}{\{\text{viscous effects}\}} = \frac{\rho\Delta p L^2}{(\eta_s+\eta_p)^2} = 0,$$
$$\mathrm{We} = \frac{\{\text{elastic effects}\}}{\{\text{viscous effects}\}} = \frac{\lambda\Delta p/7.17}{\eta_s+\eta_p} = 5,$$
$$\beta = \frac{\{\text{solvent viscous effects}\}}{\{\text{total viscous effects}\}} = \frac{\eta_s}{\eta_s+\eta_p} = 0.59$$
and $a_{\max}{}^2 = 100,$

where the dimensionless Reynolds number Re, Weissenberg number We, and solvent to viscosity ratio β have been introduced, the meaning of which have been explained with $\{\ldots\}$ meaning "magnitude of". A Newtonian fluid is recovered in the limit of We going to zero or β going to 1. $\beta = 0.59$ is a standard within benchmarking of numerical algorithms as it is a typical value for dilute polymer solutions, while $\mathrm{We} = 5$ and $a_{\max}{}^2 = 100$ represents an upper limit for steady solutions.

As illustrated in fig. 2, we find a contraction obstacle design regardless of whether we impose a horizontal symmetry line or not (a-b). The working mechanism relates to a strand of elongated dumbbells, which appears in the obstacle wake. The accelerating nature of the flow in this region causes the forward dumbbell mass to move faster than the rear mass, which causes extension in the spring between them (c-d). This mechanism is particularly strong in the hard flow configuration, where it gives rise to a local velocity minimum along the line connecting the contractions (e-g).

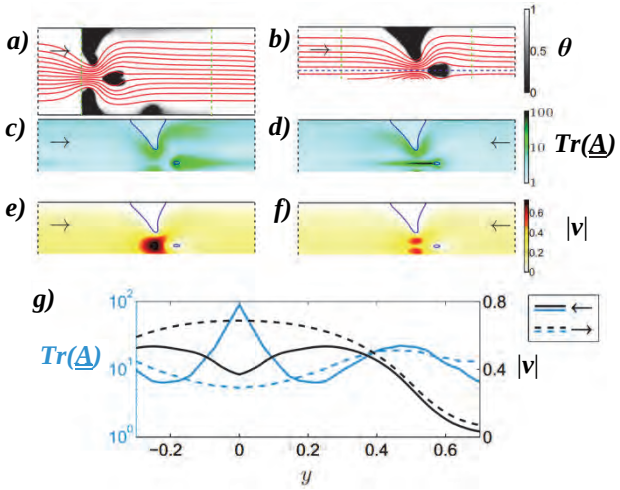

Figure 2. Results of topology optimization of anisotropic flow resistance is shown without and with an impose symmetry line in (a) and (b), respectively. The effects of the design on the conformation tensor trace and velocity are shown in (c-g) for both flow directions.

To rule out the effect of the damping term, we perform simulations for a contraction obstacle design as well as a hyperbolic contraction design as shown in fig. 3. The contraction obstacle design appears to be superior in the regime of low elasticity, but experiments with contraction designs have revealed flow rate ratios of 2 and higher in the regime of high elasticity. This is due to early presence of elastic turbulence (and thus high dissipation) for the hard flow direction. This constituted our motivation for performing experiments with the contraction obstacle design in the regime of high elasticity.

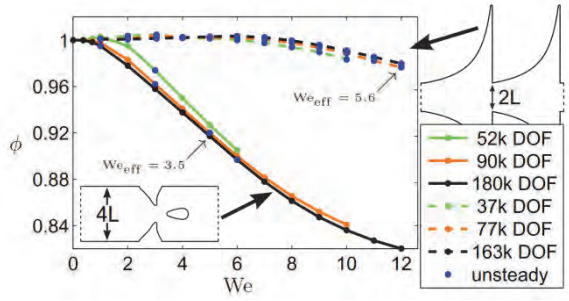

Figure 3. Two designs are compared in terms of flow rate ratio as a function of We. Effective Weissenberg numbers We_{eff} are calculated based on the average inlet velocity in the easy (→) flow direction.

EXPERIMENTS WITH NEW DESIGN

The notation related to the experimental results differs from the optimization in the sense that

$$\mathrm{We} = \lambda \frac{v_{\mathrm{avg}}}{L} = \lambda \frac{2\dot{V}}{L_{\mathrm{cont}}^2 h}, \text{ and}$$

$$\phi = \Delta p_{\mathrm{easy}} / \Delta p_{\mathrm{hard}},$$

where h is the channel depth. That is the Weissenberg number is defined in terms of the average flow velocity in the contraction rather than the driving pressure, while half the contraction width is taken as the characteristic length scale. Furthermore the objective function is based on driving pressure with values larger than one corresponding to rectification in the expected direction. Fig. 4 illustrates the channels fabricated in PDMS using standard soft lithography techniques. We use standard differential pressures with limited sensitivity, so we have to repeat each unit 25 times, which also results in approximate periodic flow conditions. The out-of-plane channel depth was 200 µm, so contrary to the optimizations, effects from the third dimension cannot be ruled out.

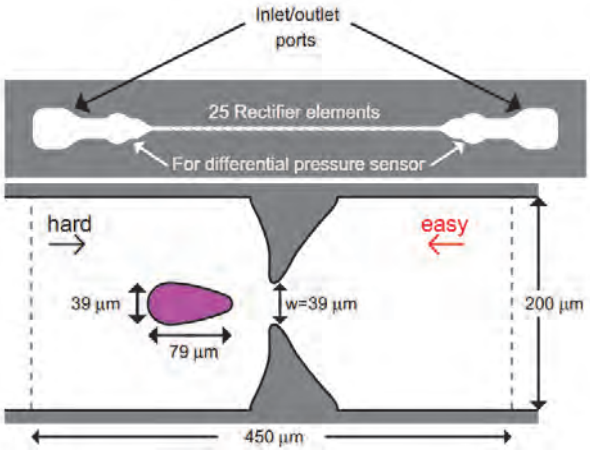

Figure 4. The overview (top) shows the channel geometry with inlet/outlet and pressure sensor ports, while the zoom up (lower) details the dimensions of each repeated unit.

For the fluid we use a dilute, 50 ppm, solution of polyacrylamide (PAA) with a molecular weight of 18 x 10^6 g/mol. We add 1 wt.% NaCl to prevent shear thinning 0.1 wt.% sodium dodecyl sulphate (SDS) to prevent blocking.

Fig. 5 shows ϕ vs. We, and it illustrates that that we were not able to completely eliminate the effect of blocking, but it is possible to identify a plateau for the objective function around 3 at $\mathrm{We} = 30$.

We performed streakline photography as shown in fig. 6, and for $\mathrm{We} = 40$ this reveals recirculations upstream of the contraction as it is usual for viscoelastic

flow in contraction geometries. The presence of the obstacle means that the flow is squeezed in the hard flow direction, which probably contributes to the working mechanism at high elasticity.

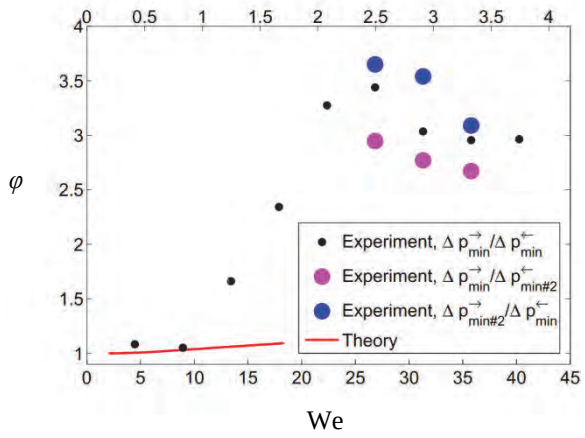

Figure 5. The driving pressure ratio is plotted versus the We number with the big blue and pink markers as indication of uncertainty due to blocking.

We were unable to compare theory and experiments in the sense that the working mechanism identified in simulations could not be observed using streakline photography, nor could we perform pressure drop measurements at low elasticity with an accuracy that would allow for comparison with simulations.

Note that a rectifier based on a contraction and an obstacle has been simulated and tested for Newtonian fluids by Tsai et al.[14], but this relied on recirculations related to the obstacle rather than the contraction. Although the steamlined shape of our obstacle would generate marginal recirculations for a Newtonian fluid, the contractions would very likely produce downstream recirculations at high Reynolds numbers, and one could thus use an enlarged version of our geometry as a valve for Newtonian fluids – although the hard and easy directions would be interchanged compared to Tsai et al.[14] as well as the viscoelastic case.

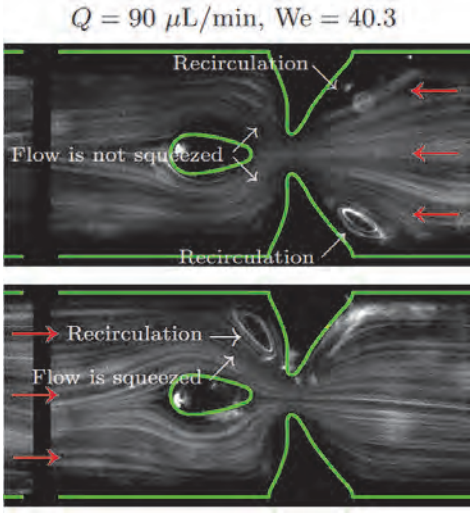

Figure 6. Streakline photography for the two flow directions at high elasticity. Note how the recirculations upstream of the contraction squeeze the flow at the obstacle in the case of the hard flow direction.

OPTIMIZATION OF BISTABILITY

The cross-slot geometry is shown in fig. 7 with a forced horizontal symmetry axis for the design, inlets to the sides and outlets in the upper and lower channels.

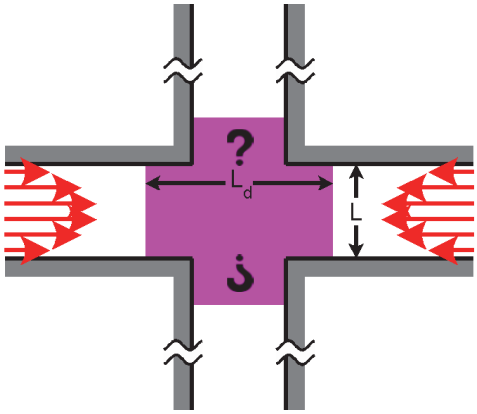

Figure 7. The cross-slot geometry is illustrated with the design area in pink and the channel width as characteristic length scale. The distance from the center to the inlet is *2L*, while it is *4L* for the outlet.

At a critical driving pressure the system goes through a pitchfork bifurcation as illustrated in fig. 8.

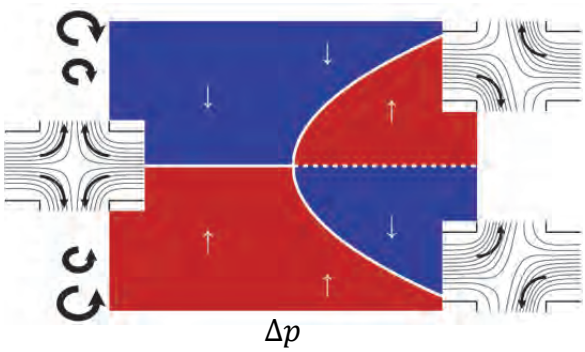

Figure 8. A pitchfork bifurcation is illustrated with rotation as solution variable on the *y*-axis. Red and blue areas give rise to increasing clock- and counterclockwise rotation, respectively. The insets show the symmetric and two asymmetric solutions at their respective position in the diagram.

When the system is forced in an unstable symmetric solution, it gives rise to an increased hydraulic resistance and thus smaller dissipation as illustrated in fig. 9. Note that the dissipation would be increasing in the case of a flow rate driven setup. The point of bistability appears implicitly in the solution, so it is not straightforward to optimize for this. We opt for a heuristic approach based on the dissipation ratio between the two states, i.e.

$$\phi = P_{\text{asym}}/P_{\text{sym}},$$

That is we hope to decrease the critical driving pressure by pulling apart the two curves in fig. 9.

Keeping the other parameters identical to the optimization of anisotropic flow resistance, fig. 10 shows the results with

$$\text{We} = \frac{\lambda \Delta p/33.6}{\eta_s+\eta_p} = 1.5 \text{ and } \beta = 0.2.$$

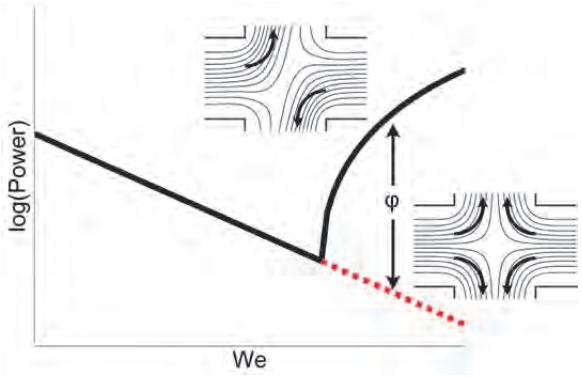

Figure 9. The logarithm of the power dissipation is sketched as a function of the driving pressure for the asymmetric (black) and symmetric flow solution (red). The distance between the two curves, ϕ is the ratio between the power dissipation in the two states.

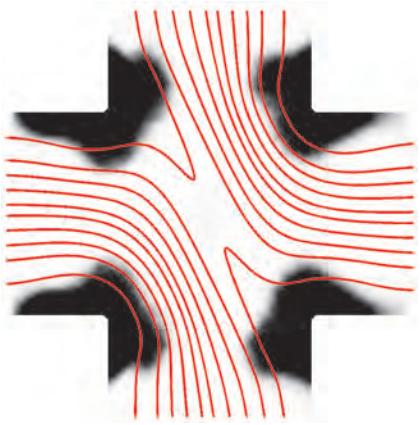

Figure 10. Topology optimization of the cross-slot for maximum dissipation ratio gives rise to contractions in the corners.

It is not surprising that the optimization produces contractions, since this increases the effective We. The contractions keep growing as long as it increases the shear rate, but at some point the pressure driven nature of the system becomes active in the sense, that the flow rate begins to drop. It thus seems that the contraction width goes to zero for increasing length of the outlet channels.

As shown in fig. 11 we once again perform simulations without the damping

term to verify that the working mechanism does not rely on it. Note that these simulations are performed by slowly ramping down We:

$$\mathrm{We} = \mathrm{We}_{\max} + \mathrm{st}(t)(\mathrm{We}_{\min} - \mathrm{We}_{\max}),$$

where $\mathrm{st}(t)$ is a regularized step function with a width of $1000\mathrm{We}_{\max}$. The figure plots We numbers, $\mathrm{We}_{\dot{V}}$ based on the flow rates for easier comparison with literature, but based on personal correspondence with Rocha et al.[11], we believe their results were based on the FENE-MCR model, so in fact no reference exists for the FENE-CR model.

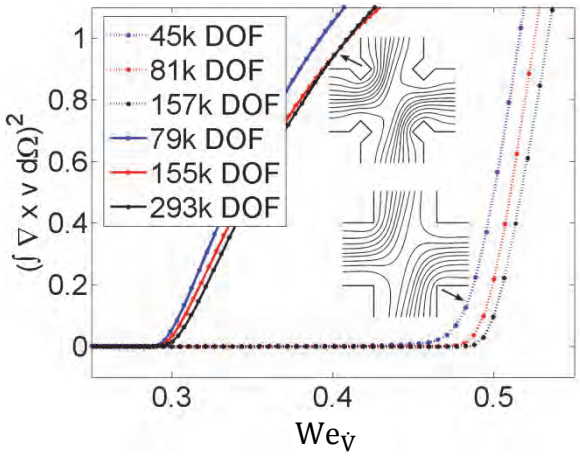

Figure 11. The integral of the vorticity is plotted as a function of We for two designs.

REFERENCES

1. Baaijens, F. et.al. (1997), "Viscoelastic flow past a confined cylinder ...", *J. of Non-Newtonian Fluid Mech.*, **68**(2), 173-203.

2. Fattal, R. and Kupferman, R. (2005), "Time-dependent simulation of viscoelastic flows at high Weissenberg number …", *J. of Non-Newtonian Fluid Mech.*, **126**(1), 23-37.

3. Olesen, L.H. et al. (2006), "A high-level programming-language...", *Int. J. for Num. Meth. in Eng.*, **65**(7), 965-1001.

4. Sahin, M. (2013), "Parallel Large-Scale Numerical Simulations of …", *J. of Non-Newtonian Fluid Mech.*, **195,** 46-46.

5. Stemme, E. and Stemme, G. (1993), "A valveless diffuser/nozzle-based …", *Sensors and Actuators A: physical*, **39**(2), 159-167.

6. Nguyen, N. et al. (2008), "Improvement of rectification effects …", *Biomicrofluidics* **2**(3), 034101.

7. Jensen, K.E. et al. (2012), "Topology optimization of viscoelastic rectifiers", *Appl. Phys. Lett.*, **100**(23), 234102.

8. Jensen, K.E. et al. (2012), "Experimental characterisation of a novel viscoelastic rectifier ...", *Biomicrofluidics*, **6**, 044112.

9. Galindo-Rosales, F. et al. (2012), "Microdevices for extensional rheometry of low viscosity …", *Microfluid Nanofluid.*

10. Arratia, P. et al. (2006), "Elastic Instabilities of Polymer Solutions in ...", *Physical Review Letters*, **96**, 144502.

11. Rocha, G. et al. (2009), "On extensibility effects in the cross-slot flow bifurcation", *J. of Non-Newtonian Fluid Mech.*, **156**, 58-69.

12. Lazarov, B. and Sigmund, O. (2011), " Filters in topology optimization based on Helmholtz-type differential…", *Int. J. for Num. Meth. in Eng*, **86**(6), 765—781.

13. Svanberg, K. (1987), " The method of moving asymptotes—a new …", *Int. J. for num. meth. In engng.*, **24**(2), 359-373.

14. Tsai, C. et al. (2012), "Formation of recirculation zones in a…", *Microfluidics and nanofluidics*, **12**(1), 213-220.